

Analyzing and Improving Conductive Networks in Commercial High-Energy Ni-rich Cathodes

Adrian Lindner^{+, [a]}, Svenja Both^{+, [b, c]}, Wolfgang Menesklou,^[a] Simon Hein,^[b, c] Timo Danner,^[b, c] Arnulf Latz,^[b, c, d] and Ulrike Krewer^{*[a]}

Nickel-rich stoichiometries such as NMC811 have gained increasing relevance for lithium-ion-batteries in recent years due to their high specific capacity and reduced use of critical resources. However, low intrinsic electronic conductivity of NMC active materials makes the use of carbon-based additives necessary. Volume fraction and distribution of the carbon-binder-domain (CBD) have a significant impact on the electrode performance. This work combines high-resolution tomography and microstructure-resolved simulations to characterize the three-dimensional transport networks of a commercial NMC811

cathode. FIB-SEM tomography reveals that low CBD volume fractions with suboptimal distribution cause a non-percolating conductive network in the microstructure and thus unfavourably low electronic conductivity. Increasing the CBD content through virtual electrode design enables percolation and enhances electronic conductivity fundamentally. Simulations on both the real and virtually designed structures demonstrate how percolating CBD networks lead to a significantly improved energy density.

1. Introduction

To meet the demands set by an ever increasing electrification of the mobility sector, lithium-ion batteries must provide higher energy and power densities. While cobalt free chemistries such as lithium-iron-phosphate (LFP) exist and gain increased attention, layered oxides such as lithium-nickel-manganese-cobalt-oxide (NMC) with a trend towards Ni-rich stoichiometries like NMC811 or even higher are still the most prominent due to their high discharge capacity.^[1]

Like most cathode active materials (CAM), NMC suffers from poor intrinsic electronic conductivity.^[2] Electronic transport inside the electrode is therefore usually enabled via conductive additives such as graphite,^[3] carbon black (CB),^[4] carbon-nanotubes (CNTs),^[5,6] graphene^[7,8] or a combination thereof. However, while a lot of work has been invested in studying the influence of these different carbonaceous species, as well as

electrode formulation and processing,^[9,10] the detailed three-dimensional distribution and morphology of the conductive network is often neglected.

In order to study the three-dimensional conductive additive network, accurate imaging-techniques^[11] are required that are able to resolve effects on the nanometer scale while providing enough volume to be representative for the entire electrode. X-ray based techniques such as lab-based micro and nano-CT^[12-14] as well as synchrotron^[15] tomography are capable in resolving the active material in the electrode structure and are widely used. They are non-destructive and offer a high range of potential applications in battery research. However, the carbon-binder-domain (CBD) is not directly accessible and requires the use of correlative techniques^[16,17] to be considered in the digital twin. Prifling et al. have shown a compilation of different correlative segmentation approaches recently, further enabling the consideration of CBD inside x-ray tomography obtained datasets.^[18]

In contrast, focused-ion-beam scanning-electron-microscopy (FIB-SEM) tomography is a destructive imaging technique able to achieve much higher resolutions. During the slice & view process, sequential surface milling and imaging provides a stack of SEM images which can then be processed into a three-dimensional structure.^[19] However, this also limits the methodology in terms of observable volume due to the restricted amount of milling as well as the limited field of view of electron microscopy detectors. In contrast to purely x-ray based imaging, identification of carbonaceous additives is possible with the right preparation techniques. Cooper et al. introduced a method of intermittent platinum deposition into the pore space to distinguish it from the CBD.^[20] While this method provides very large and contrast-rich cross sections, the tomographic uses are limited since the process was not yet automated and slice thickness could not be controlled precisely. Ender et al. were one of the first to show a full three phase FIB-SEM


[a] A. Lindner,⁺ Dr.-Ing. W. Menesklou, Prof. Dr.-Ing. U. Krewer
 Institute for Applied Materials - Electrochemical Technologies, Karlsruhe
 Institute of Technology, 76135 Karlsruhe
 E-mail: ulrike.krewer@kit.edu


[b] S. Both,⁺ Dr. S. Hein, Dr. T. Danner, Prof. Dr. A. Latz
 German Aerospace Center (DLR), Institute of Engineering Thermodynamics,
 Stuttgart, Germany

[c] S. Both,⁺ Dr. S. Hein, Dr. T. Danner, Prof. Dr. A. Latz
 Helmholtz Institute Ulm for Electrochemical Energy Storage (HIU), Ulm,
 Germany

[d] Prof. Dr. A. Latz
 Institute of Electrochemistry, Ulm University, Ulm, Germany

[⁺] These authors contributed equally.

 Supporting information for this article is available on the WWW under
<https://doi.org/10.1002/batt.202400503>

 © 2024 The Authors. Batteries & Supercaps published by Wiley-VCH GmbH.
 This is an open access article under the terms of the Creative Commons
 Attribution License, which permits use, distribution and reproduction in any
 medium, provided the original work is properly cited.

tomography of lithium-ion-battery electrodes.^[21] Their methodology of infiltration with contrast-rich resin is still used to date^[22] and a modified version is also used in the present work. Besnard et al. utilized FIB-SEM tomography to characterize different NMC/LFP compositions including the CBD on the microscale and in a limited volume. They point out a need for studies on CBD connectivity and attachment between CBD and CAM.^[23]

Each cathode has a complex microstructure consisting of active material, pore space,^[24] conductive additives^[25,26] and binders^[27] in order to function properly. Therefore, the microstructure of an electrode has a significant impact on the performance of the cell.^[28] Almar et al. successfully used FIB-SEM tomography to investigate the cathode microstructures of commercial cells. Similarly to other previous studies they focus on volumes smaller than the electrode thickness.^[29] Additionally, results are not linked to electrochemical behavior, and structurally induced performance limitations are not assessed. In a recent two-part study, Cadiou et al. show the importance of CBD connectivity. They point out that larger volumes are needed in order to fulfill the requirements of a representative volume element (RVE) which they achieve by correlating FIB-SEM and x-ray based techniques.^[30,31] Our study presented in the following highlights the importance of covering the entire electrode thickness with FIB-SEM tomography when attempting to understand how the microstructure will limit discharge performance.

While imaging techniques are an important tool to study the structure of electrodes, adding simulative studies to the investigation can significantly improve the mechanistic understanding of the structures and the limitations induced by them. Chen et al. presented an extensive characterization followed by simulations in a the framework of a Doyle-Fuller-Newman (DFN) Model^[32] for a NMC811/graphite cell. This modeling approach uses effective transport parameters,^[32,33] thus making it an efficient and fast tool to use. Laue et al. used virtually generated microstructures to parameterize a robust homogenized P2D model and quantify structure-property correlations in lithium-ion-battery electrodes.^[34] The influence of CBD is thereby often lumped together with the effective electrode conductivity and not treated individually.^[32,33] While investigating the impact of CBD on the electrode performance can be included in these homogenized approaches,^[35] local inhomogeneities arising from the distribution in the microstructure are hard to capture in DFN type models. Xu et al. investigated NMC622 cathodes via x-ray tomography with subsequent 3D microstructure-resolved simulations assuming a homogenized electrolyte-CBD phase with effective transport parameters.^[36] Since it has been shown that both the amount of carbon-binder-domain (CBD)^[37] as well as its distribution and morphology^[38] are of great importance for the performance of a cell, fully microstructure-resolved models are needed to take into account inhomogeneities in the CBD distribution. One approach to study the 3D-resolved CBD and its impact on electrode performance is to use generated microstructures. Joos et al. introduced a virtual microstructure generation based on a database of real active material and CBD particles.^[39] These generated structures can then in turn be

used to perform simulative studies on the electrode level.^[40] Recently, the combination of structure-resolved simulation and deep learning to predict an optimized microstructure and the corresponding processing procedure has been shown by Marcató et al.^[41] While the mentioned approaches are valuable for their respective application, simulative approaches that take into account both the real distribution of CBD as well as the real electrode structure obtained from high-resolution imaging techniques are needed. Otherwise, inhomogeneous distribution or insufficient addition of additives during the manufacturing process cannot be captured.

In this study we investigate a commercially available electrode in order to understand current limitations as well as improve electrode design for future development. Hence, obtaining a real microstructure containing spatially resolved information about the CBD is crucial. This requires both a high-resolution tomography as well as microstructure-resolved simulations to predict the performance. Our work presents an improved tomography method, which allows for resolving the CBD phase in the electrode while still covering the entire thickness (80 μm) of a commercial high-energy cathode. The electrode reconstruction from the tomography is then used as an input for a 3D microstructure-resolved electrochemical continuum model to study the performance of the electrode, especially the effect of CBD distribution and CAM conductivity. This way we eliminate the need for correlative or generative approaches and can consider the as-observed CBD distribution as well as the real microstructure in our simulations. We demonstrate the necessity for an improved FIB-SEM tomography by investigating the effect of dataset volume on both microstructural parameters as well as simulation results. Afterwards, we unveil performance limitations which arise from a suboptimal conductive network and tackle these limitations through morphological optimization.

With an improved tomographic method and insight into the importance of conductive binder networks in nickel-rich cathodes, the approach is shown to enable the virtual improvement of the electrode microstructure. While such optimization is often performed using virtually generated electrode structures, we start with real data of a commercially available cathode thereby probing simple strategies to increase the achievable energy density in high-energy cathodes to guide future development of such materials.

2. Results and Discussion

Representative Volume and Size Effects

Two FIB-SEM datasets with different overall volume and resolution were obtained from the same cathode in order to investigate resolution and size effects. Since the volume of a tomographic dataset is always coupled to its resolution, the size and resolution needs to be tailored to the respective scientific question. Here, we compare a partial reconstruction which does not include the full thickness of the electrode to a full reconstruction with a thickness of 77 μm . The partial reconstruc-

tion is shown in Figure 1a. It provides insight into a volume of $79200 \mu\text{m}^3$ with a resolution of 50 nm. It covers 62.5% of the total electrode thickness, which was measured as 80 μm in tactile measurements.

As a comparison, a second FIB-SEM tomography covering $137000 \mu\text{m}^3$ of volume as well as the full electrode thickness is shown in Figure 1b. The significantly larger volume obtained at a resolution of 88 nm is mainly enabled by using a thick protective multilayer between the porous electrode and the Ga^+ -beam to prevent inhomogeneous milling, also known as curtaining.^[42] An image of the prepared sample including the multilayer coating is provided in Figure S6. More details on sample preparation and experimental procedure can be found in the experimental section.

To assess whether both tomographic approaches offer a similarly representative three-dimensional electrode structure we calculate the theoretical capacity of the cathode based on both structures and compare it to the capacity measured in quasi open circuit voltage (qOCV) half cell experiments. We use the measured active material stoichiometry as well as the mass loading derived from the tomographic data to obtain the capacities. Details on the calculation are provided in the experimental section.

The calculated capacity of the full tomography (5.59 mAh cm^{-2}) is in much better agreement to the experimentally obtained value (5.57 mAh cm^{-2}) compared to the partial tomography (6.63 mAh cm^{-2}). It appears that a partial tomography of the given electrode is not representative. A reason for this could be inhomogeneities along the electrode thickness which are only covered by performing a tomography of the full electrode thickness.

Since the processed FIB-SEM data is directly used as the simulation domain in this work, only the simulation on 3D data

covering the entire electrode thickness will yield meaningful results.

Cathode Microstructure

We used the software toolbox GeoDict (2023 & 2024 Release)^[43] to evaluate transport properties of the 3D structure provided by the full tomography. Results of the quantification are given in Table 1 and details on evaluation are provided in the experimental section. As stated above, conductive additive networks play an important role in determining the performance of active material chemistries with low intrinsic electronic conductivity such as NMC. Therefore, we investigate CBD properties beyond the volumetric content, also accounting for distribution, connectivity and percolation. The CBD content of 3.41 vol.-%, coupled with a low connectivity of 67% leads to no percolating pathways between separator and current collector. The results of the connectivity and distribution analysis are visualized in Figure S7 and S8, respectively. In general, full percolation is achieved if pathways of CBD continue from the separator side to the current collector. We use an algorithm for pathfinding in voxelized 3D data implemented in the MatDict module of GeoDict 2023 to search for percolating electronic pathways through the CBD. For the given electrode structure, no percolating paths through the electrode were found. A visualization of the CBD is given in Figure 2a. As CBD percolation is crucial for the electronic transport, the impact on electronic conductivity of the cathode structure will be evaluated further. Effective electronic conductivity is obtained using a structurally resolved approximation approach described in the methodological section of this work. The structure shows low effective electronic conductivity of only 0.24 S m^{-1} due to the non-percolating CBD network, which in itself is a result of low CBD content and connectivity. We verified this result with four different tomographies and found none of them showing percolation paths through the CBD.

In summary, microstructural evaluation based on FIB-SEM tomography data of the cathode suggests that an unoptimized carbon-binder-domain leads to a non-percolating conductive network and ultimately low electronic conductivity. This is in line with previous observations made on virtual electrode structures^[38,44]. We will explore the impact of this microstructural feature on electrode performance in the simulation section.

Carbon-Binder-Domain Optimization

To fully understand the influence of the additive network towards evidence-based electrode design, we virtually optimize the carbon-binder-domain inside the original electrode structure obtained via FIB-SEM tomography. To overcome hindered electronic transport without introducing severe limitations to ionic transport in the electrolyte we virtually added CBD in 1 vol.-% steps to the original microstructure and tracked the effective electronic conductivity as well as the pore diffusivity.

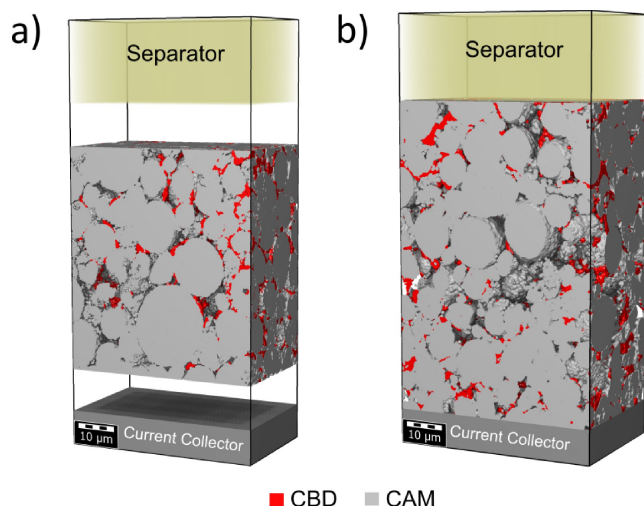


Figure 1. Three-dimensional models of the investigated positive electrode based on FIB-SEM tomography. (a) Partial tomography with an investigated volume of $79200 \mu\text{m}^3$. Only about 2/3 of the electrode thickness are included in this tomography, leading to a less representative dataset. (b) Full tomography including the entire electrode thickness and an investigated volume of $137000 \mu\text{m}^3$.

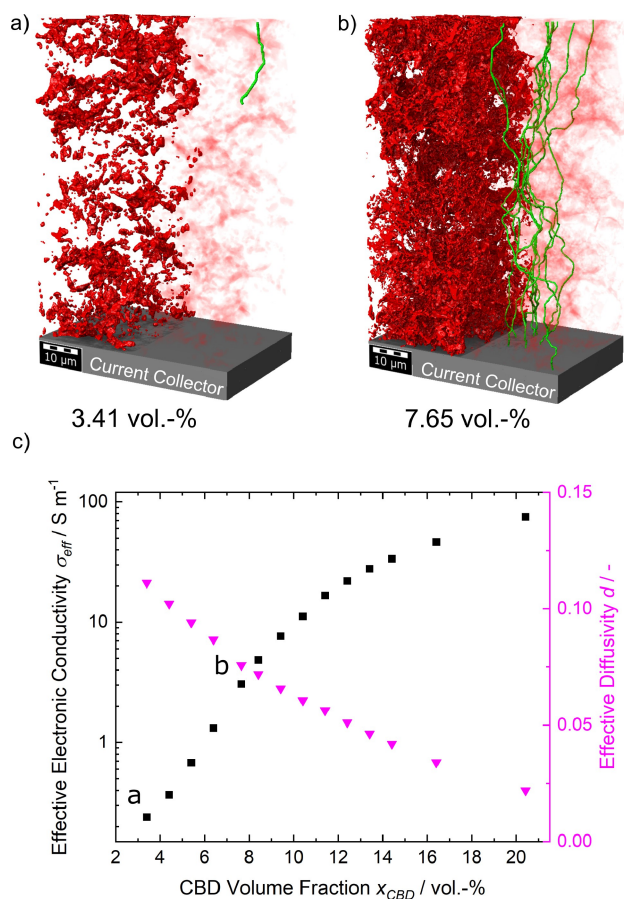


Figure 2. Visualization and influence of CBD distribution and percolating electronic pathways. Lower CBD contents of 3.41 vol.-% lead to a non-percolating conductive network in the electrode microstructure obtained via FIB-SEM tomography (a) Original structure with CBD colored red and exemplary pathways in green. Active material is not shown. (b) NMC811 electrode with optimized CBD content of 7.65 vol.-% resulting in percolating pathways across the electrode thickness. (c) Correlation between effective electrode conductivity, effective pore diffusivity and volumetric CBD content in the structure. Electrode conductivity initially shows a strong increase until percolation is established. After percolation is reached and connected pathways of CBD are present, conductivity increase slows down. Addition of CBD is stopped at 20 vol.-% since diffusivity approaches 0.

The algorithm and settings used for virtual binder modification are outlined in the experimental section. The results are shown in Figure 2c. Initially, we observe a strong increase in electronic conductivity until percolating pathways are introduced between 7 to 8 vol.-% CBD. As soon as percolation is established, the increase in conductivity becomes less prominent. For further characterization and simulative investigation we chose a structure with 7.65 vol.-% CBD; Figure 2b reveals significantly more percolating pathways than the original structure with 3.41 vol.-% CBD in Figure 2a.

When comparing the homogenized microstructural parameters in Table 1, a clear increase in CBD connectivity, percolation and, as a result, effective electronic conductivity is observed. And since the active material particle structure has undergone no changes, we can conclude that increasing CBD content leads to higher connectivity, improved percolation and ultimately, better electronic conductivity.

	Unoptimized CBD	Optimized CBD
x_{CBD} / vol.-%	3.41	7.65
x_{AM} / vol.-%	70.43	70.43
x_{Pore} / vol.-%	26.16	21.91
CBD connectivity C_{CBD} / -	0.67	0.91
CBD percolation / -	No	Yes
Effective electronic conductivity σ_{eff} / S m ⁻¹	0.24	3.06
Pore tortuosity factor τ_{pore}^2 / -	2.51	3.40

Since CBD is added only into the pore space, this will reduce effective ionic transport properties in the electrolyte. To assess transport properties in the pore space we again employ a structurally resolved approximation approach implemented in the DiffuDict module of GeoDict and calculate the tortuosity factor τ_{pore}^2 of the pore space. The effective diffusivity d is a dimensionless value which describes the influence of the porous media on the ionic transport properties of the electrolyte. It is defined according to Equation 1 based on Epstein:^[45]

$$d = \frac{x_{pore}}{\tau_{pore}^2} \quad (1)$$

Here, x_{pore} is the porosity and τ_{pore} the tortuosity of the pore space. This includes the homogenized microporosity inside the CBD which is also considered during electrochemical continuum simulation. Details of the approach can be found in the experimental section of this work and results are shown in Table 1. The change in effective pore space diffusivity during CBD addition is shown in Figure 2c. A decrease with increasing CBD content can be observed and is attributed to a loss of pore space after adding CBD. Diffusivity approaches 0 beyond 20.4 vol.-% CBD. For the chosen optimized structure with 7.65 vol.-%, the tortuosity factor increases by about 35% from 2.51 to 3.40. A lower effective diffusivity suggests additional ionic transport losses in the structure with optimized CBD, which might become relevant at higher current densities.

Microstructure-Resolved Simulation

In this section, 3D microstructure-resolved simulations in the framework BEST are performed on both the cathode structure obtained through the full FIB-SEM tomography as well as the modified structure with an increased volume fraction of 7.65 vol.-% CBD.

First, the impact of the FIB-SEM based reconstruction volume discussed in Section 2 was evaluated through simulations on the partial and full electrode structure. Both structures were used to perform a discharge simulation at a low current density of 0.56 mA cm⁻² (0.1 C) and are compared to experimentally obtained discharge curves. Virtual half-cells

consist of a lithium counter electrode, a homogenized separator, the respective cathode structure and a current collector on each side. Simulation details are provided in the Methods Section and in the Supporting Information. Our simulation in Figure S2 shows a very high discharge capacity ($> 6 \text{ mAh cm}^{-2}$) for the partial tomography at a very low current density of 0.56 mA cm^{-2} (C/10). This confirms that the active material content is overestimated in this tomography and not representative for the whole structure as the small region of interest cannot account for inhomogeneities across the entire electrode. In contrast, simulations on the full (large volume) tomography data show very good agreement with experimental data across the entire cathode potential. The small current density has been chosen for a comparison of both structures as the discharge capacities are not strongly influenced by transport or kinetic parameters at such a low current.

To summarize, our simulative analysis is in line with the capacity calculations discussed above, which show good agreement only for the full tomography. Therefore, only the full FIB-SEM tomography structure will be used for further simulative investigation.

Original CBD Structure

To gain insight into the discharge behaviour of the commercial cathode, we conduct rate performance simulations and compare them to experimental data of half-cell measurements. A comparison between the simulated half-cell curves and the corresponding measurements for current densities between 0.56 mA cm^{-2} (C/10), 2.79 mA cm^{-2} (C/2), 5.57 mA cm^{-2} (1 C) and 11.15 mA cm^{-2} (2 C) is shown in Figure 3. Our simulation approach is able to predict the discharge capacities with a very good agreement especially for the lower current densities up to

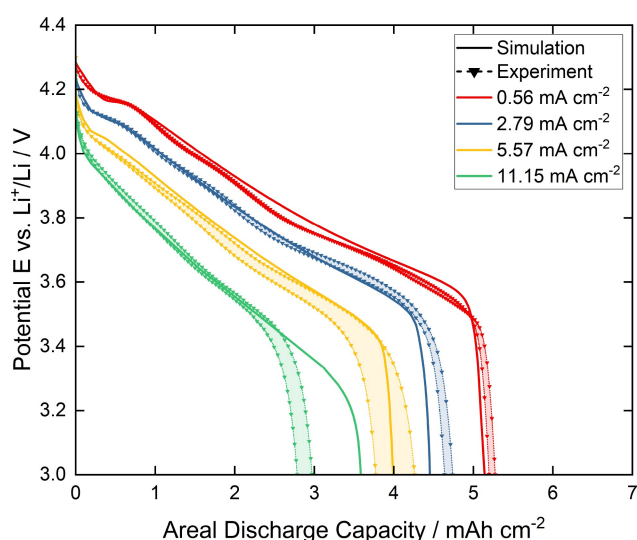


Figure 3. Simulative (solid lines) and experimental (shaded regions between markers) discharge curves of the cathode for current densities between 0.56 and 11.15 mA cm^{-2} . Experimental results have been measured eight times per current density and minimum and maximum values are shown for each current density.

5.57 mA cm^{-2} (1 C). For 11.15 mA cm^{-2} , a larger deviation between simulation and experiment is observed, which might be caused by uncertainties in the model calibration, e.g. the chemical diffusion coefficient of the CAM. Further discussion on different diffusion coefficients is provided in the Supporting Information. Note that small deviations in the capacities are expected especially for the low currents since the reconstructed volume had to be cropped by $3 \mu\text{m}$ compared to the measured thickness of approximately $80 \mu\text{m}$ to avoid edge effects in the image processing. We estimate a decrease in capacity of $\sim 3.75\%$ due to this image processing step.

Since our simulation framework provides us with spatially and temporally resolved concentration profiles, we can have a closer look at the state-of-charge (SOC), i.e. state of lithiation, at the end of discharge (3 V). SOC denotes the lithium concentration in each voxel with respect to the maximum concentration c_{max} as provided in the Supporting Information. SOC distributions for current densities of 0.56 mA cm^{-2} (C/10), 5.57 mA cm^{-2} (1 C) and 11.15 mA cm^{-2} (2 C) as well as corresponding 2D cutouts of the middle plane are shown in Figure 4. The left side of each image is adjacent to the separator and the right side adjacent to the current collector. Astonishingly, for 0.56 mA cm^{-2} (C/10) a very inhomogeneous lithiation is observed across the thickness of the electrode with a higher state of lithiation at the current collector. This indicates a reduction in achievable capacity due to the electronic conductive network inside the electrode. Low-resistive electron transport is only possible in close proximity to the current collector, enabling preferential lithiation in this part of the electrode. The low amount of CBD as well as its non-percolating distribution, c.f. Figure 2a, enforces (at least partly) electronic conduction through the active material. Since the active material conductivity is orders of magnitude lower than the one of the homogenized CBD phase, only minor electron transport can take place. The good agreement with the experimental data, further supported by the observation of no percolating net-

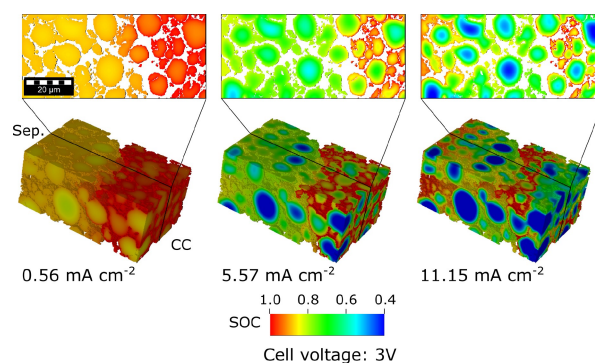


Figure 4. State-of-charge (SOC) profiles at the end of discharge with current densities of 0.56 mA cm^{-2} (0.1 C), 5.57 mA cm^{-2} (1 C) and 11.15 mA cm^{-2} (2 C), simulated on the full tomography. The left and right side of each structure are adjacent to the separator (Sep.) and current collector (CC), respectively. SOC is defined as local lithium concentration in the active material divided by the maximum lithium concentration. A strong inhomogeneity in concentration can be observed across the electrode for 0.56 mA cm^{-2} and 5.57 mA cm^{-2} , indicating an electronic limitation of the performance.

work, clearly points towards a performance limitation of the cathode due to electronic transport. This effect is even more pronounced for 5.57 mA cm^{-2} (1 C). At the highest current density of 11.15 mA cm^{-2} (2 C), a different behaviour occurs with a high degree of lithiation both near the separator and the current collector. A higher state of lithiation close to the separator hints towards an ionic transport limitation of the discharge process. In case of insufficient ionic transport, ions can not be delivered fast enough and less intercalation in the part close to the current collector is possible. However, the concentration profile indicates that at high rates, both electronic and ionic transport limit the CAM utilization.

Since we observe an electronic limitation of the performance for lower current densities, which is most likely induced by the poor percolation of the CBD, we now compare our as-reconstructed cathode to the virtual sample with an increased CBD content. Given the increased electronic conductivity, c.f. Table 1 of the optimized electrode, we want to investigate if a higher CBD content can improve the discharge performance in the following Section.

Optimized CBD Structure

The C-rate performance of the half-cell discharge simulations on the optimized structure with 7 vol.-% CBD and the as-reconstructed cathode structure are given in Figure 5. We want to point out that all model parameters are kept identical to the simulations obtained on the original microstructure and only the CBD distribution and content was adjusted. We find a capacity improvement between 8% for C/10 (0.56 mA cm^{-2}) and even 18% for 5.57 mA cm^{-2} (1 C). This is clearly due to the significantly improved conduction network in the optimized electrode, providing percolating electronic networks across the

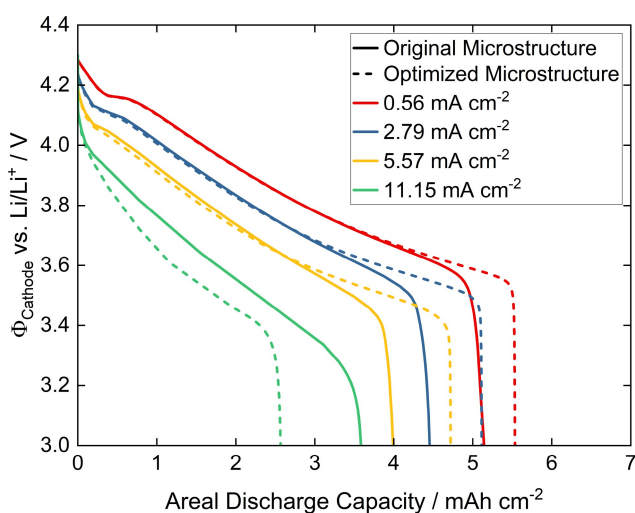


Figure 5. Simulated cathode rate performance for discharge current densities between 0.56 mA cm^{-2} and 11.15 mA cm^{-2} for the original structure and the modified structure with ~ 7 vol.-% CBD. A significant increase in achievable capacity is observed for low to medium current densities (max. 18% at 5.57 mA cm^{-2}). For current densities of 11.15 mA cm^{-2} (2 C) and above, capacity retention is decreased due to limited ionic transport.

whole structure as discussed earlier and shown by the connectivity analysis in the Supporting Information. SOC distributions at the end of discharge presented in Figure 6 show a much more homogeneous state of lithiation compared to the original case (c.f. Figure 4) and thus a higher active material utilization. For 5.57 mA cm^{-2} (1 C), the homogeneous utilization is even more distinct than for C/10, which is clearly visibly from the concentration distribution. A small degree of lithiation can only be observed in the large particles due to the Li diffusion in the active material while the rest of the electrode is lithiated homogeneously. However, for the highest current density of 11.15 mA cm^{-2} (2 C), the achieved capacity of the optimized structure is found to be even lower than for the original structure. This is also evident from the 11.15 mA cm^{-2} (2 C) SOC distribution in Figure 6, where the region close to the current collector is at a very low state of lithiation while the electrode part close to the separator is already at a very high degree of lithiation.

In contrast to the as-reconstructed electrode, the optimized electrode design is limited by transport of lithium ions through the electrolyte for C-rates of 2 C or higher. As discussed in Section 2, pore tortuosity increased significantly through addition of ~ 4 vol.-% CBD, which leads to the observed transport hindrance. Note that this cell is designed for high-energy application and should not be cycled with high current densities as the maximum continuous current density recommended by the manufacturer is 1.5 C. Therefore, the improvements due to electronic conductivity at low current densities up to 5.57 mA cm^{-2} (1 C) outweighs the performance loss at high currents. Note that this virtual optimization cannot be validated experimentally as we are investigating commercially available material. This highlights the need for workflows combining imaging techniques and simulation tools as shown in this work in order to further improve material design in cases in which experimental testing is difficult and expensive.

In summary, we observed a limitation of the performance in the original cathode structure due to the poor electronic conductive network and that the capacity for current densities up to 5.57 mA cm^{-2} (1 C) could be significantly increased

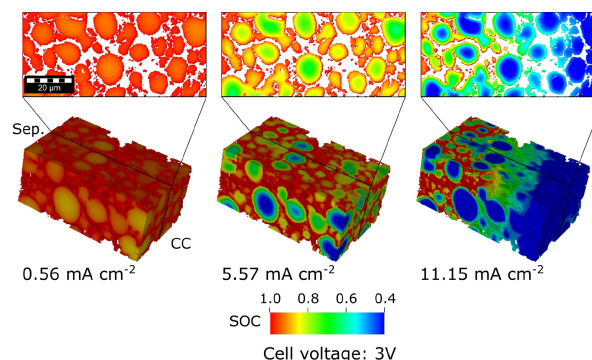


Figure 6. State-of-charge (SOC) profiles after discharge with current densities of 0.56 mA cm^{-2} (0.1 C), 5.57 mA cm^{-2} (1 C) and 11.15 mA cm^{-2} (2 C) for the optimized binder structure. A more homogeneous lithiation can be observed for C/10 and 1 C, while an ionic limitation of the 11.15 mA cm^{-2} (2 C) discharge capacity is observed.

through addition of only 4 vol.-% CBD. Focussing on the gravimetric energy densities (see SI for bulk densities and calculation), the optimized structure has an energy density of 659.53 Wh kg⁻¹ compared to 576.26 Wh kg⁻¹ at 5.57 mA cm⁻² (1 C). The additional CBD increases the energy density by roughly 14% even though additional inactive material is used.

3. Conclusions

Starting from a commercially available lithium-ion battery, we show a combined tomography and simulation approach for characterization and optimization of positive electrodes for high-energy cells. The microstructure is investigated via FIB-SEM tomography, utilizing a protective multilayer Pt/carbon/Pt coating for large volumetric imaging. This reveals inhomogeneities across the electrode thickness as well as volume content and distribution of the CBD. The so obtained digital twin enables precise capacity predictions by 3D microstructure-resolved simulations of the electrode and proves the necessity for representative electrode volumes. We conclude that such large volumetric imaging is crucial for the understanding and virtual optimization of real electrode structures.

Another key observation is that low CBD contents and the absence of percolating networks limit the performance even at small C-Rates. The absence of a percolating electron conducting network leads to a low overall electrode conductivity, resulting in poor discharge performance. The non-percolating conductive network was confirmed by analyzing CBD distribution, connectivity and three-dimensional path analysis. Adding CBD into the real structure using virtual electrode design establishes percolation and increase electronic conductivity. Through microstructure-resolved simulations, we show how optimizing this network by enabling electron percolation through the CBD can increase the 1 C areal discharge capacity by up to 18% as well as gravimetric energy density by up to 14%. However, ionic transport properties in the electrolyte are adversely affected by adding CBD due to a loss of pore space and increase in tortuosity, resulting in reduced performance at very high current densities. Therefore, this work emphasizes the importance of conductive carbon networks in the positive electrode as well as tools that enable their quantification and predict the resulting electrode performance. Ensuring percolation of conductive networks without severely hindering ionic transport is identified as a key design goal for electrode manufacturing. Future work in this field will focus on structurally resolved simulation and optimization approaches containing both electrodes, thereby enabling the virtual design of the whole cell.

Experimental

Cell Opening and Electrode Extraction

Electrodes from a commercially available Lithium-Ion-Battery (nominal capacity 4850 mAh, LG-Chem INR21700 M50T) were used for

the model-assisted tomographic and electrochemical analysis. The cells were fully discharged to 2.5 V at C/20 (0.24 A) before cell disassembly in a glovebox under a protective gas atmosphere (< 1 ppm water/oxygen, MBraun, Germany). After opening, cathode sheets were cut out and subsequently dipped in dimethyl carbonate (DMC) in order to wash off any electrolyte residue. Then, the DMC was drained off and electrodes were dried for 1 hour inside the glovebox. As the electrode sheets were coated with active material on both sides, one side was removed by carefully brushing off the coating using N-Methyl-2-pyrrolidone (NMP, Sigma-Aldrich, Germany) as a solvent inside the glovebox. Subsequently, the electrodes were subjected to a drying process at 110 °C for at least 4 hours. To build experimental cells, cathode sheets were punched to a circular shape with a diameter of 1.8 cm (surface area of 2.54 cm²) using the EL-Cut high-precision electrode cutter (EL-Cell, Germany). The punched electrodes were washed with DMC again to eliminate small particles which may form as a result of punching.

Half-Cell Assembly

To assess discharge performance, punched electrodes were assembled in a half cell configuration with lithium metal as a counter electrode inside an Ar-filled glovebox. Before cell assembly, the cell components were dried for at least 12 hours at 110 °C. The three electrode half cell configuration was composed of a PAT-cell housing (EL-Cell, Germany) the extracted cathode, the lithium metal counter electrode, a lithium ring reference electrode (EL-Cell, Germany), a glass fiber separator (glass microfiber filter, uncompressed thickness of 0.21 mm, VWR, Germany) and 150 μL electrolyte (1 M LiPF₆ in EC/EMC 50/50 (v/v), Sigma-Aldrich, Germany).

Discharge Performance

All electrochemical experiments were conducted using a BaSyTec CTS-Lab (BaSyTec GmbH, Germany). Experimental cells were placed inside a 25 °C climate chamber (ESPEC LU-114, ESPEC Europe GmbH, Germany). Using the experimental half cell, a 0.01 C discharge was conducted between 4.3 V and 3.0 V against the lithium reference. The so obtained capacity was used to set current densities for rate performance measurements. Using the same upper and lower voltage limit, constant-current performance of the cathode was evaluated for discharge current densities between 0.56 mA cm⁻² (0.1 C) and 11.15 mA cm⁻² (2 C). Charging was performed with a constant-current density of 1.12 mA cm⁻² (0.2 C). To ensure reproducibility, four measurements were conducted per current density in two separate cells, thus eight measurements per current density in total. Figure 3 shows minimum and maximum values for each current density with all other curves falling into the shaded area between.

Physico-Chemical Analysis

The crystal structure of the cathode active material was investigated using x-ray diffraction (XRD) (D8 Advance, Bruker, Germany). To achieve high spectral quality, parts of the cathode coating were carefully separated from the current collector and measured on a silicon waver with a rotational speed of 3 min⁻¹ to avoid background noise. A copper tube was used as the x-ray generator with a voltage of 40 kV and a current of 40 mA. The two-theta range of 10 to 90 degrees was measured to collect the full spectra. Evaluation was conducted using Diffraction EVA (Bruker, Germany) by subtracting the Cu K α background followed by noise removal. The results match with reference spectra of NMC811.^[46] Active material composition was obtained using energy dispersive x-ray spectro-

scopy (EDX). Measurements were conducted inside a scanning electron microscope (1540 XB, Zeiss Microscopy, Oberkochen, Germany) equipped with an EDX system (Quantax, Bruker AXS, Germany). To ensure high spectral quality and avoid the influence of carbon additives, measurements were conducted on particle cross sections which were milled using the integrated focused ion beam system. An acceleration voltage of 20 kV was used and results were aggregated from multiple point measurements. Quantitative evaluation was performed using Bruker Esprit. SEM micrographs were obtained inside the same SEM using an acceleration voltage of 1.3 kV.

FIB-SEM Tomography

For FIB-SEM tomography, the cleaned cathode extracted from the full cell was cut to a size of 5 x 5 mm and vacuum infiltrated using a two-component silicon resin (Elastosil R604B, Wacker Chemie, Germany). After curing the resin for 48 h the cathode was fixed to a sample holder and sputtered with a thin (<15 nm) platinum coating inside a low vacuum sputter coater (EM ACE200, Leica, Germany). In order to ensure high image quality and low milling artifacts during the large volume tomography, an additional dual-material layer was deployed on top of the sample. In a first step, a two-component carbon adhesive (M-Bond, Micro Measurements, Germany) was drip coated and hardened inside a 60 °C dry-chamber for 48 h. Subsequently, an additional layer of platinum (< 15 nm) was sputtered on top. This ensures both milling quality across the entire thickness as well as high electronic conductivity of the sample to prevent charging effects during imaging. After finding a region of interest (ROI) inside the scanning electron microscope (1540 XB, Zeiss Microscopy, Oberkochen, Germany), the sample was moved into the coincident as well as the eucentric point. That way the automatic focus is able to maintain optimal image quality. Trenches were milled with the integrated Ga⁺-ion source using a beam current of 10 nA. The trenches are necessary to avoid redeposition of milled material onto or close to the ROI. The Slice&View process is performed using a lower current of 2 nA resulting in a finer beam. Images were obtained using an acceleration voltage of 1.3 kV and collection time of 90 s. A voxel size of 88 nm was chosen to account for the very large ROI of the high volume tomography. Cubic voxels were ensured by setting the spacing of milled surfaces to 88 nm. In total, 1600 images were taken during the process. For the low-volume tomography a smaller pixel size of 50 nm was chosen. Adjusting the mill spacing to 50 nm resulted in 700 overall images taken.

Image Processing

Images obtained via FIB-SEM tomography underwent extensive processing before and after segmentation in order to reliably quantify the cathode material. Initially, an algorithm based on scale invariant feature transform^[47] implemented in ImageJ was used to align sequential images. After cropping the region of interest, remaining curtaining artifacts were removed using a GeoDict^[43] feature based on the work of Fitschen et. al.^[48] Curtaining results from inhomogeneous sputtering rates due to differences in sample topography.^[42] In order to successfully segment the cathode into three phases i.e. active material, pore space and carbon-binder-domain, images were first filtered using anisotropic diffusion as well as greyscale gradient removal. Both features are implemented in ImageJ. Afterwards, three phase segmentation using grey values was performed and the 3D structure was post-processed in two steps. Firstly, unconnected components of the solid phase (<1000 voxel) were removed to reduce noise. Afterwards, morphological closing was used to remove artifacts introduced by three phase

segmentation. Finally, the 3D representation of the cathode micro-structure is used for quantitative analysis as well as simulation.

Binder Modification

The addition of carbon-binder-domain into the voxelized structure was performed using the ProcessGeo module in GeoDict 2023.^[49] The AddBinder function was used and 1 vol.-% increments were added into the structure using no anisotropy settings and a default contact angle setting of 0°. These settings guarantee a random distribution of CBD without preferential orientation or location.

Calculation of Theoretical Capacities

Both tomographic datasets were processed, segmented and evaluated for areal loading I_{areal} and volumetric phase content of the three phases active material x_{AM} , carbon binder domain x_{CBD} and porosity x_{Pore} . The volumetric phase content is defined according to equation 2, where n_{AM} is the number of voxels assigned to the active material after segmentation and n_{total} is the overall number of voxels in the dataset.

$$x_{AM} = \frac{n_{AM}}{n_{total}} \quad (2)$$

The volumetric active material content for partial and full tomography are 0.81 and 0.70, respectively. With gravimetric densities for both active material and carbon binder domain, we used the digital material laboratory GeoDict^[43] to calculate the areal loading I_{areal} of both datasets as well as the gravimetric active material content $x_{AM,wt.}$ of both active material and CBD. The areal loading of active material is then obtained through Equation 3.

$$I_{areal,AM} = I_{areal} \cdot x_{AM,wt.} \quad (3)$$

The active material loading of the partial and full tomography are 30.1 mg cm⁻² and 25.9 mg cm⁻², respectively. Next, we calculated the specific gravimetric capacity of the active material according to equation 4.

$$c_{gravimetric} = \frac{zF}{M_{AM}} \quad (4)$$

Here, the number of transferred electrons z was assumed to be 0.8 since the observed voltage range of 3.0 to 4.3 V allows to use 80% of the theoretical capacity. The molar mass of the active material was calculated following equation 5.

$$M_{AM} = M_{Li} + x_{Ni}M_{Ni} + x_{Mn}M_{Mn} + x_{Co}M_{Co} + 2M_{O_2} \quad (5)$$

Active material crystal structure was determined via x-ray diffraction (XRD) measurements and matches with NMC spectra from literature.^[46] The stoichiometry is measured using energy dispersive x-ray spectroscopy (EDX). Finally, areal capacity for both electrodes was calculated with equation 6.

$$c_{areal} = \frac{zF}{M_{AM}} \cdot I_{areal,AM} \quad (6)$$

Modeling and Simulation

Microstructure-resolved simulations were conducted in the framework BEST.^[50] The governing equations shown in Table 2 describe both charge and mass transport in the active material and the electrolyte derived from non-equilibrium thermodynamics.^[51] Active material and electrolyte are coupled by a charge transfer process in parallel with a double layer current at the respective interface. The faradaic current i_{TBV} is modelled by the expression derived by Latz et al.^[52] The double layer current is modelled as proposed in [38] with the double layer capacity C_{DL} and $\Delta\Phi$ as the difference between the solid potential Φ_{so} and the electrochemical potential in the electrolyte φ_{el} .^[38] Due to the application of a finite-volume scheme, the governing equations are directly solved on the reconstructions of the tomography data obtained through FIB-SEM tomography. The tomography data is already voxelized and assigns a specific phase (e.g. Active Material, Pore Space, Carbon-Binder-Domain) to all voxels, which act as the finite volumes for the discretization. Since the carbon-binder-phase is observed as one phase in the tomography and not separated into carbon black (or any other conductive agent) and binder, we assume a homogenized carbon-binder-domain (CBD) consisting of electrolyte and a carbon-binder-phase without resolving the binder and carbon black individually. As the tomography is able to quantify the CBD phase accurately, we inherently take into account its distribution in the structure. Porous CBD is considered by solving governing equations for charge transport in the solid phase as well as charge and mass

transport in the electrolyte phase for each CBD voxel with effective transport parameters. The effective transport parameters of the electrolyte part of the CBD are calculated using the following equation to relate them to the respective bulk properties:

$$\chi_{\text{eff}} = \frac{X_{\text{Pore,CBD}}}{\tau_{\text{Pore,CBD}}} \cdot \chi_{\text{bulk}} \quad (9)$$

Here, χ denotes either the ionic conductivity in the electrolyte phase κ or the chemical diffusion coefficient D of Li-ions in the homogenized phase. The effective electronic conductivity in the CBD can be described with the same form of equation, but due to the significantly higher electronic conductivity of the CBD phase (compared to the active material) its effective conductivity is equal to the bulk conductivity of conductive agent in our simulations ($\frac{\chi}{\tau} = 1$).

For computational runtime reasons, the high volume structure has been rescaled by a factor of 2. This was done using the Rescale Algorithm in the ProcessGeo module in GeoDict (Math2Market, Germany), which yields a voxel size of 176 nm instead of 88 nm. The influence of resizing on the structure as well as on the simulation results is discussed in the Supporting Information.

The half-cell used for our simulation study consists of a lithium counter electrode, a homogenized separator, our cathode structure and an electrolyte (1 M LiPF₆ in EC:EMC). All parameters used in this study can be found in the Supporting Information. Discharge simulations were conducted following the experimental procedure, starting at a lithium concentration of 0.010312 mol cm⁻³ in the active material, which equals a half-cell voltage of 4.3 V, applying current densities between 0.56 mA cm⁻² and 11.15 mA cm⁻².

Effective electronic electrode conductivity at 50% SOC was calculated using the ConductoDict module in GeoDict 2023 (Math2Market, Germany). Bulk properties for active material and CBD are specified in Table 1 in the Supporting Information. The tortuosity of the porous network was calculated similarly using the DiffuDict module in GeoDict 2023. Laplace diffusion (Knudsen number $\ll 1$) was assumed and Dirichlet boundary conditions were used for all calculations. For our calculations we assume the effective transport values given in the Supporting Information.

Table 2. Governing equations for the simulations in BEST.	
Active material	
Mass balance:	$\frac{\partial c_s}{\partial t} = -\nabla \cdot (-D_s \nabla c_s)$
Charge balance:	$0 = -\nabla \cdot i_s$
Electr. current:	$i_s = -\sigma_s \nabla \Phi_s$
Electrolyte	
Mass balance:	$\frac{\partial c_e}{\partial t} = -\nabla \cdot (-D_e \nabla c_e + \frac{t_{Li^+} i_e}{F})$
Charge balance:	$0 = -\nabla \cdot i_e$
Ionic current:	$i_e = -\kappa_e \nabla \varphi_e - \kappa_D \nabla c_e$ $\kappa_D = \kappa_e \frac{(t_{Li^+} - 1)}{F} \left(\frac{\partial \mu_e}{\partial c_e} \right)$
Carbon-Binder-Domain (CBD)	
Electrolyte fraction:	
Mass balance:	$\frac{\partial c_e}{\partial t} = -\nabla \cdot (-D_{e,\text{eff}} \nabla c_e + \frac{t_{Li^+} i_e}{F})$
Charge balance:	$0 = -\nabla \cdot i_e$
Ionic current:	$i_e = -\kappa_{e,\text{eff}} \nabla \varphi_e - \kappa_{D,\text{eff}} \nabla c_e$ $\kappa_{D,\text{eff}} = \kappa_{e,\text{eff}} \frac{(t_{Li^+} - 1)}{F} \left(\frac{\partial \mu_e}{\partial c_e} \right)$
Solid fraction:	
Charge balance:	$0 = -\nabla \cdot i_s$
Electr. current:	$i_s = -\sigma_{s,\text{eff}} \nabla \Phi_s$
Interface	
Faradaic current:	
$i_{\text{TBV}} = 2 i_{00} \sqrt{c_{\text{El}}} \sqrt{c_{\text{so}}} \sinh\left(\frac{F}{2RT} \eta\right)$	
Overpotential η :	
$\eta = \Phi_{\text{so}} - \varphi_{\text{el}} - U_0(c_{\text{so}})$	
Double layer current:	
$i_{\text{DL}} = -C_{\text{DL}} \frac{d\Delta\Phi}{dt}$	
Interface current:	
$i_{\text{SE}} = i_{\text{BV}} + i_{\text{DL}}$	

Acknowledgements

The authors thankfully acknowledge funding by the German federal ministry of education and research through the project "MiCha" (03XP0317 B/D). The authors acknowledge support by the state of Baden-Württemberg through bwHPC and the German Research Foundation (DFG) through grant no. INST 40/575-1 FUGG (JUSTUS 2 cluster). Open Access funding enabled and organized by Projekt DEAL.

Conflict of Interests

There is no conflict of interest to declare.

Data Availability Statement

The data that support the findings of this study are openly available in KITOpen at <https://doi.org/10.35097/hsHwAgyn-DovbKTU>, reference number 1000172805.

Keywords: Carbon-Binder-Domain · Electronic conductivity · Lithium-ion batteries · Microstructure · Simulation

- [1] A. Butt, G. Ali, K. Tul Kubra, R. Sharif, A. Salman, M. Bashir, S. Jamil, *Energy Technology* **2022**, *10*, 2100775.
- [2] R. Amin, Y.-M. Chiang, *Journal of The Electrochemical Society* **2016**, *163*, A1512.
- [3] H.-Y. Tran, A. Lindner, W. Menesklou, W. Braunwarth, *Energy Technology* **2023**, *11*.
- [4] O. S. Medvedev, Q. Wang, A. A. Popovich, P. A. Novikov, *Ionics* **2020**, *26*, 4277.
- [5] P. Sehwat, C. Julien, S. S. Islam, *Materials Science and Engineering: B* **2016**, *213*, 12.
- [6] K. Sheem, Y. H. Lee, H. S. Lim, *Journal of Power Sources* **2006**, *158*, 1425.
- [7] D. Shin, H. Park, S. Lee, U. Paik, T. Song, *Industrial & Engineering Chemistry Research* **2020**, *59*, 12889.
- [8] Y. Shi, L. Wen, S. Pei, M. Wu, F. Li, *Journal of Energy Chemistry* **2019**, *30*, 19.
- [9] A. Hoffmann, E. A. Heider, C. Dreer, C. Pfeifer, M. Wohlfahrt-Mehrens, *Energy Technology* **2023**, *11*.
- [10] M. Weber, R. Moschner, A. Kwade, *Energy Technology* **2023**, *11*.
- [11] Z. Deng, X. Lin, Z. Huang, J. Meng, Y. Zhong, G. Ma, Y. Zhou, Y. Shen, H. Ding, Y. Huang, *Advanced Energy Materials* **2021**, *11*, 2000806.
- [12] M. Ender, J. Joos, A. Weber, E. Ivers-Tiffée, *Journal of Power Sources* **2014**, *269*, 912.
- [13] T. M. M. Heenan, A. Jnawali, M. D. R. Kok, T. G. Tranter, C. Tan, A. Dimitrijevic, R. Jervis, D. J. L. Brett, P. R. Shearing, *Journal of The Electrochemical Society* **2020**, *167*, 140530.
- [14] P. R. Shearing, N. P. Brandon, J. Gelb, R. Bradley, P. J. Withers, A. J. Marquis, S. Cooper, S. J. Harris, *Journal of The Electrochemical Society* **2012**, *159*, A1023.
- [15] F. Tang, Z. Wu, C. Yang, M. Osenberg, A. Hilger, K. Dong, H. Markötter, I. Manke, F. Sun, L. Chen, G. Cui, *Small Methods* **2021**, *5*, 2100557.
- [16] L. Zielke, T. Hutzenlaub, D. R. Wheeler, C.-W. Chao, I. Manke, A. Hilger, N. Paust, R. Zengerle, S. Thiele, *Advanced Energy Materials* **2015**, *5*, 1401612.
- [17] S. R. Daemi, C. Tan, T. Volkenandt, S. J. Cooper, A. Palacios-Padros, J. Cookson, D. J. L. Brett, P. R. Shearing, *ACS Applied Energy Materials* **2018**, *1*, 3702.
- [18] B. Prifling, M. Neumann, S. Hein, T. Danner, E. Heider, A. Hoffmann, P. Rieder, A. Hilger, M. Osenberg, I. Manke, M. Wohlfahrt-Mehrens, A. Latz, V. Schmidt, *Energy Technology* **2023**, *11*.
- [19] D. Kim, S. Lee, W. Hong, H. Lee, S. Jeon, S. Han, J. Nam, *Microscopy and microanalysis : the official journal of Microscopy Society of America, Microbeam Analysis Society, Microscopical Society of Canada* **2019**, *25*, 1139.
- [20] S. J. Cooper, S. A. Roberts, Z. Liu, B. Winiarski, *Journal of The Electrochemical Society* **2022**, *169*, 070512.
- [21] M. Ender, J. Joos, T. Carraro, E. Ivers-Tiffée, *Journal of The Electrochemical Society* **2012**, *159*, A972.
- [22] J. Costard, J. Joos, A. Schmidt, E. Ivers-Tiffée, *Energy Technology* **2021**, *9*.
- [23] N. Besnard, A. Etienne, T. Douillard, O. Dubrunfaut, P. Tran-Van, L. Gautier, S. Franger, J.-C. Badot, E. Maire, B. Lestriez, *Advanced Energy Materials* **2017**, *7*, 1602239.
- [24] T. Beuse, M. Fingerle, C. Wagner, M. Winter, M. Börner, *Batteries* **2021**, *7*, 70.
- [25] R. Tian, N. Alcalá, S. J. K. O'Neill, D. V. Horvath, J. Coelho, A. J. Griffin, Y. Zhang, V. Nicolosi, C. O'Dwyer, J. N. Coleman, *ACS Applied Energy Materials* **2020**, *3*, 2966.
- [26] J. Entwistle, R. Ge, K. Pardikar, R. Smith, D. Cumming, *Renewable and Sustainable Energy Reviews* **2022**, *166*, 112624.
- [27] D. Das, S. Manna, S. Puravankara, *Batteries* **2023**, *9*, 193.
- [28] J. K. Mayer, L. Almar, E. Asyubekov, W. Haselrieder, A. Kwade, A. Weber, H. Nirschl, *Energy Technology* **2020**, *8*, 1900161.
- [29] L. Almar, J. Joos, A. Weber, E. Ivers-Tiffée, *Journal of Power Sources* **2019**, *427*, 1.
- [30] F. Cadiou, T. Douillard, N. Besnard, B. Lestriez, E. Maire, *Journal of The Electrochemical Society* **2020**, *167*, 100521.
- [31] F. Cadiou, T. Douillard, F. Willot, J.-C. Badot, B. Lestriez, E. Maire, *Journal of The Electrochemical Society* **2020**, *167*, 140504.
- [32] C.-H. Chen, F. Brosa Planella, K. O'Regan, D. Gastol, W. Dhammika Widadanage, E. Kendrick, *Journal of The Electrochemical Society* **2020**, *167*, 080534.
- [33] J. Sturm, A. Rheinfeld, I. Zilberman, F. B. Spingler, S. Kosch, F. Frie, A. Jossen, *Journal of Power Sources* **2019**, *412*, 204.
- [34] V. Laue, F. Röder, U. Krewer, *Electrochimica Acta* **2019**, *314*, 20.
- [35] F. L. E. Usseglio-Viretta, A. Colclasure, A. N. Mistry, K. P. Y. Claver, F. Pouraghajan, D. P. Finegan, T. M. M. Heenan, D. Abraham, P. P. Mukherjee, D. Wheeler, P. Shearing, S. J. Cooper, K. Smith, *Journal of The Electrochemical Society* **2018**, *165*, A3403.
- [36] R. Xu, Y. Yang, F. Yin, P. Liu, P. Cloetens, Y. Liu, F. Lin, K. Zhao, *Journal of The Mechanics and Physics of Solids* **2019**, *129*, 160.
- [37] T. Knorr, S. Hein, B. Prifling, M. Neumann, T. Danner, V. Schmidt, A. Latz, *Energies* **2022**, *15*, 7821.
- [38] S. Hein, T. Danner, D. Westhoff, B. Prifling, R. Scurtu, L. Kremer, A. Hoffmann, A. Hilger, M. Osenberg, I. Manke, M. Wohlfahrt-Mehrens, V. Schmidt, A. Latz, *Journal of The Electrochemical Society* **2020**, *167*, 013546.
- [39] J. Joos, A. Buchele, A. Schmidt, A. Weber, E. Ivers-Tiffée, *Energy Technology* **2021**, *9*.
- [40] A. Schmidt, E. Ramani, T. Carraro, J. Joos, A. Weber, M. Kamlah, E. Ivers-Tiffée, *Energy Technology* **2021**, *9*, 2000881.
- [41] A. Marcato, J. E. Santos, C. Liu, G. Boccardo, D. Marchisio, A. A. Franco, *Energy Storage Materials* **2023**, *63*, 102927.
- [42] L. A. Gianuzzi, F. A. Stevie, *Micron*, **1999**.
- [43] *GeoDict Software Release 2023 from Math2Market GmbH, Germany* **2023**.
- [44] R. Ge, A. M. Boyce, Y. Sun, P. R. Shearing, P. S. Grant, D. J. Cumming, R. M. Smith, *ACS applied materials & interfaces* **2023**, *15*, 27809–27820, journal Article.
- [45] N. Epstein, *Chemical Engineering Science* **1989**, *44*, 777–779, pii: 0009250989850535.
- [46] J. Zhu, G. Chen, *Journal of Materials Chemistry A* **2019**, *7*, 5463–5474.
- [47] T. Lindeberg, *Scholarpedia* **2012**, *7*, 10491.
- [48] J. H. Fitchen, J. Ma, S. Schuff, *Computer Vision and Image Understanding* **2017**, *155*, 24.
- [49] A. Blumer, A. Streit, B. Planas, *GeoDict 2024 User Guide. ProcessGeo handbook, Math2Market GmbH, Germany*.
- [50] Fraunhofer Institute for Industrial Mathematics (ITWM), BEST—Battery and Electrochemistry Simulation Tool, <https://www.itwm.fraunhofer.de/best>, last accessed: 15.02.2024.
- [51] A. Latz, J. Zausch, *Journal of Power Sources* **2011**, *196*, 3296.
- [52] A. Latz, J. Zausch, *Electrochimica Acta* **2013**, *110*, 358.

Manuscript received: July 26, 2024

Revised manuscript received: September 20, 2024

Accepted manuscript online: September 23, 2024

Version of record online: November 9, 2024